Assessing the mechanisms of common Pb incorporation into titanite

C.L. Kirkland[a,*], D. Fougerouse[a,b], S.M. Reddy[a,b], J. Hollis[c], D.W. Saxey[b]

[a] School of Earth and Planetary Sciences (*CET Curtin Node), Curtin University, GPO Box U1987, Perth, WA 6845, Australia
[b] Geoscience Atom Probe, Advanced Resource Characterisation Facility, John de Laeter Centre, Curtin University, GPO Box U1987, Perth, WA 6845, Australia
[c] Geology Department, Ministry of Mineral Resources, Government of Greenland, P.O. Box 930, 3900 Nuuk, Greenland

ARTICLE INFO

ABSTRACT

Common Pb, the portion of non-radiogenic Pb within a U bearing mineral, needs to be accurately accounted for in order to subtract its effect on U-Pb isotopic ratios so that meaningful ages can be calculated. The propensity to accommodate common Pb during crystallization, or later, is different across the range of U bearing minerals used for geochronology. Titanite frequently accommodates significant amounts of common Pb. However, the most appropriate method to correct for this requires knowledge on the mechanism and timing of common Pb incorporation; information that is commonly difficult to extract. In this study, the spatial and compositional distribution of trace elements (including Pb) in metamorphic titanites from a Greenland amphibolite is investigated on the grain- to nano-scale. Titanites have an isotopically similar signature for both common and radiogenic-Pb in all grains but significantly different quantities of the non-radiogenic component. Microstructural and compositional examination of these grains reveals undeformed, but high common Pb (F207%) titanites have homogeneous element distributions on the atomic scale suggesting common Pb is incorporated into titanite during its growth and not during later processes. In contrast, deformed titanite comprising low-angle boundaries, formed by subgrain rotation recrystallization, comprise networks of dislocations that are enriched in Mg, Al, K and Fe. Smaller cations may migrate due to elastic strain in the vicinity of the dislocation network, yet the larger K cations more likely reflect the mobility of externally-derived K along the orientation interface. The absence of Pb enrichment along the boundary indicates that either Pb was too large to fit into migrating lattice dislocations or static low-angle boundaries and/or that there was no external Pb available to diffuse along the grain boundary. As the common Pb composition is distinctly different to regional Pb models, the metamorphic titanite grew in a homogeneous Pb reservoir dominated by the break-down of precursor U-bearing phases. The different quantity of common Pb in the titanite grains indicates a mineral-driven element partitioning in an isotopically homogeneous metamorphic reservoir, consistent with low U, low total REE and flat LREE signatures in high F207% analyses. These results have implications for the selection of appropriate common Pb corrections in titanite and other accessory phases.

1. Introduction

Titanite ($CaTiSiO_5$) is a reactive mineral that frequently grows from other phases, or recrystallizes, during metamorphism and as such is a useful geochronometer for tectonometamorphic studies. However, titanite often incorporates significant amounts of common Pb; that is Pb not produced by in-situ radiogenic decay within the dated mineral (e.g. Aleinikoff et al., 2002; Marsh and Smye, 2017). Goldschmidt's rules provide a useful context for understanding the nature of common Pb in titanite; Pb^{2+} readily substitutes for Ca^{2+} in the titanite structure, yet Pb diffusivity in titanite is relatively slow. Hence, much of the common Pb cargo of titanite is predicted to be a function of that trapped during mineral growth rather than diffused into the mineral, although it should

also be considered that Pb can exist in the Pb^{4+} state which has an ionic radius of only 0.78–0.94 Å, making it a possible candidate for admission into the lattice (Kramers et al., 2009). However, the role of structural defects in facilitating Pb mobility and entrapment in titanite has not be extensively explored, though it has been considered important in other U-Pb chronometers (Piazolo et al., 2016; Peterman et al., 2016).

Both the amount and composition of common Pb can vary significantly depending on the local crystallization environments as indicated by inter- and intra- grain variability (e.g. Romer and Rötzler, 2003). There are a range of options for correcting for this common Pb component to calculate meaningful radiogenic-Pb ages (e.g. Storey et al., 2006; Chew et al., 2014). However, the choice of the most appropriate common Pb correction depends on an understanding of the

composition of the common Pb, which in turn frequently requires that we know the time of common Pb incorporation into the grain. Many methods for common Pb correction make an assumption about either, or both, the quantity and composition of the common Pb component. For example, in performing a ^{204}Pb correction, the composition of common Pb is assumed to vary with age of the sample (from uncorrected ratios) following terrestrial Pb evolution models. Hence, an assumption on the *composition* of common Pb is made. Other correction approaches, such as a regression through an uncorrected dataset, assumes perfect concordance; that is, an assumption about the *quantity* of common Pb is made (e.g. Gibson and Ireland, 1996). Other mechanisms for correcting for common Pb assume that coexisting low-U phases (such as feldspar), rich in the common Pb component, have the same common Pb composition as the mineral of interest, which may not ubiquitously be the case (Wohlgemuth-Ueberwasser et al., 2017). Furthermore, the composition of Pb in the growth reservoir may be significantly dissimilar from typical crustal Pb model compositions (e.g. Stacey and Kramers, 1975), particularly when U and Th bearing precursor minerals are involved in the generation of the titanite (Romer, 2001; Romer and Siegesmund, 2003; Kirkland et al., 2017).

In many situations, the choice of common Pb correction is dictated by the analytical approach taken. In LA-ICPMS systems, accurate ^{204}Pb measurements can be challenging due to ^{204}Hg interference in the He carrier gas (but see Horstwood et al., 2003). Moreover, the inferred mechanism and timing of common Pb incorporation into a mineral will dictate the most appropriate common Pb correction strategy. That is, common Pb may be regarded as ancient and incorporated into the crystal during its growth, alternatively common Pb may be regarded as modern - perhaps derived from laboratory or other geologically recent contamination. Each of these scenarios could result in different best estimates of the likely common Pb composition.

Discriminating between the different mechanisms and timing of common Pb incorporation into minerals has clear implications on the choice of common Pb correction method and hence best practice for U-Pb geochronology. In this work, we present a case study aimed at identifying the mechanism of common Pb incorporation into metamorphic titanite crystals in mafic amphibolites of the Karrat Group, Greenland. We apply a combination of electron backscattered diffraction (EBSD) and atom probe microscopy (APM) to investigate the nanoscale distribution of trace elements and Pb associated with pristine and deformed parts of the titanite crystal lattice.

2. Geological setting

Titanite from mafic lavas of the Kangigdleq Member, Nûkavsak Formation, Karrat Group are used as a case study to explore common Pb incorporation in this mineral. The Karrat Group lies in the southernmost Rae Craton within the Rinkian Fold Belt (Escher and Pulvertaft, 1976). The Rae Craton has been inferred to have acted as a long standing upper plate onto which numerous other crustal fragments were emplaced during orogenic events throughout the Proterozoic (Hoffman, 1990). One of these orogenic events spawned the Rinkian Fold Belt in West Greenland at c. 1.88 Ga (Sanborn-Barrie et al., 2017). The Karrat Group crops out in the Uummannaq region and extends northward to the Melville Bugt. The group consists of shallow shelf, largely clastic rocks of the Qeqertarssuaq Formation and the grey-wacke-flysch-dominated Nûkavsak Formation (Henderson and Pulvertaft, 1967; Grocott and McCaffrey, 2017). The Qeqertarssuaq Formation has been correlated with the Mârmorilik Formation which displays an angular unconformity to c. 3.0 Ga Archean crystalline basement (Garde, 1978; Henderson and Pulvertaft, 1987; Connelly and Thrane, 2005). The Nûkavsak Formation consists of a succession of turbiditic metasedimentary rocks including minor carbonate, quartzite and mafic metavolcanic rocks metamorphosed at greenschist to amphibolite facies, with minor local granulite facies exposures (Henderson and Pulvertaft, 1967; Henderson, 1969; Pulvertaft, 1973). The youngest

detrital zircon in the Nûkavsak Formation indicate the rocks were deposited after 1.9 Ga (Sanborn-Barrie et al., 2017) and the same rocks are interpreted to have been intruded by the Prøven Igneous Complex and pegmatites at 1869 ± 9 Ma (Thrane et al., 2005). A previous study of magmatic apatite and metamorphic titanite in the Nûkavsak Formation documented U-Pb ages of 1826 ± 9 Ma and 1768 ± 8 Ma respectively (Kirkland et al., 2017). The apatite ages were interpreted to reflect total resetting in an event at temperatures > 485 °C, whereas the titanite date was interpreted as the age of new metamorphic growth. The resetting of the U-Pb system in magmatic apatite was linked to the collision between the Rae and the Superior Cratons during the Trans-Hudson Orogeny, whereas subsequent metamorphic titanite growth was interpreted as distal evidence of an event associated with the Nagssugtoqidian Orogeny. On the basis of these findings, a shared tectonic history for over 100 million years between the Nagssugtoqidian and Rinkian Orogens was proposed (Kirkland et al., 2017).

Titanites were extracted from medium-grained amphibolites of the Kangigdleq Member, Nûkavsak Formation. These intensely foliated amphibolites contain volcanic textures including pillows and hyaloclasite tuffs (Grocott and Vissers, 1984) and are interpreted as metamorphosed mafic lavas and tuffs. The rocks are dominated by prismatic black amphibole (1–3 mm) and plagioclase (1–2 mm) that define the foliation. Chlorite and muscovite occurs parallel to the foliation (Fig. 1). Clinopyroxene is rarely observed and where present appears partially broken down and wrapped by the amphibole-plagioclaise (+chlorite, +muscovite) fabric. Titanite post-dates clinopyroxene. The rocks also contain the following U-bearing accessory minerals, in order of abundance; titanite, apatite, calcite, perovskite, and rutile. The foliation in the rocks is correlated with the regional D_2 phase which produced NE-vergent thrusts and the main metamorphic fabric across the area.

2.1. Geochronological context

Previously U-Pb dated metamorphic titanite, growing within the D_2 foliation, was chosen to explore the nature of common Pb in relation to microtextures and nanochemistry. This titanite yields a U-Pb age younger than magmatic apatite in the same rock and, on the basis of isotope diffusion modelling, could not have exceeded 452 °C, nor been subject to thermally-activated Pb diffusion (Kirkland et al., 2017). The published U-Pb data from titanite of the Nûkavsak Formation yields U-Pb isotopic data that scatters along a regression between a common Pb component with ^{207}Pb/^{206}Pb ratio of 0.813 ± 0.068 (MSWD = 2.3) and a radiogenic component that yields an age of c. 1770 Ma (Fig. 2),
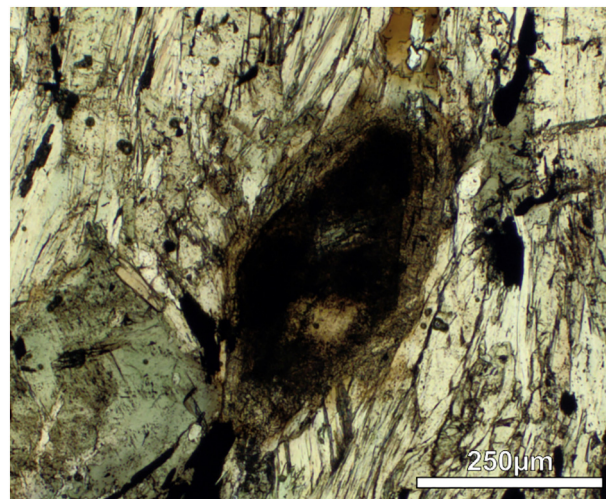

Fig. 1. Thin-section photomicrograph showing the relationship of euhedral titanite to chlorite, amphibole, muscovite, plagioclase, and opaque oxide minerals. Titanite interleaved with muscovite, amphibole, and chlorite.
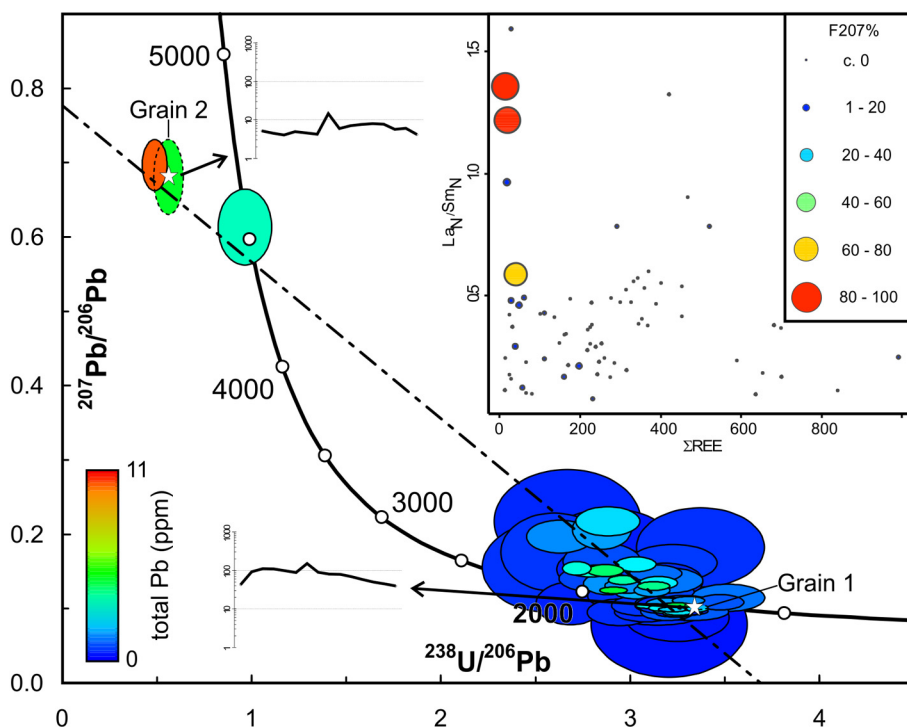
Fig. 2. Tera-Wasserberg concordia diagram for titanite from sample 570128, Karrat Group, Greenland (after Kirkland et al., 2017). Error ellipses are at the 2 sigma level and coloured according to total Pb concentration. Grain 1 and Grain 2, investigated in this work, are denoted by overlaid stars. Inset is a plot of LaN/SmN (chondrite normalized) versus total REE content with data point circles coloured and scaled according to F207%. The inset REE profiles are REE chondrite normalized plots for grains 1 and 2.

interpreted to date the metamorphic crystallization of the titanite (Kirkland et al., 2017). The regression through all data has scatter in excess of that which can be accounted for by solely analytical uncertainties and could indicate some degree of radiogenic-Pb loss and/or variable common Pb composition. Nonetheless, two other samples of titanite from this formation also show a similar $^{207}Pb/^{206}Pb$ value for their upper intercepts, implying a regionally consistent common Pb reservoir was accessed by titanite. Four analyses (three with geochemistry presented in this work) plot at distinctly elevated $^{207}Pb/^{206}Pb$ ratios with a tendency to reverse discordance. These analyses when considered as a discrete group yield a similar upper intercept on a Tera and Wasserberg plot, consistent with them also incorporating common Pb from this reservoir.

The large spread in relative F207 affords an excellent opportunity to evaluate potential causes of dispersion along a common – radiogenic mixing array: that may be due to either variable common Pb quantity or an unchanged common Pb concentration but variable U content. The upper intercept from a U-Pb regression through this U-Pb data is distinctly lower than c. 1770 Ma common Pb (e.g. $^{207}Pb/^{206}Pb_c$ 1770 Ma = 0.98) predicted by regional Pb evolution models. No change in common Pb signature was observed with laser ablation time, hence surface-derived contamination was not considered feasible (Kirkland et al., 2017). Given the low $^{207}Pb/^{206}Pb$ ratio for the titanite common Pb component, two alternatives appear possible:

1) Common Pb has been incorporated into the crystal structure through pathways that have remained open to isotopic exchange after crystallization.
2) The common Pb in the titanite reflects a mixture between different regional common Pb reservoirs including radiogenic-Pb from a precursor U bearing phase.

Both alternatives would have predictable consequences on the micro and nano scales. For example, if recent Pb exchange has taken place, it would principally be facilitated through transport pathways into the grain such as brittle fractures or low- and high-angle boundaries associated with crystal plasticity. Alternatively, if the common Pb represents a homogenously distributed component that has mixed with

a radiogenic precursor during grain crystallization, then no relationship between Pb and transport pathways should necessarily exist. The aim of this study is to test these two models through the integration of LA-ICPMS compositional analysis, electron microscopy (BSE, EBSD) and Atom Probe Microscopy (APM), to investigate the relationship between deformation microstructures, trace element distribution (including Pb) and the isotopic composition of Pb. APM is used because it is able to analyse compositional heterogeneity in deformation-related microstructures (Reddy et al., 2016; Piazolo et al., 2016). In addition, APM studies examining the Pb composition of zircon crystals have shown that several, isotopically distinct, Pb reservoirs, with geologically meaningful ages, can be preserved within nanoscale domains (Valley et al., 2014; Valley et al., 2015; Peterman et al., 2016). Such nanoscale imaging of the Pb isotopic signature in zircon has provided fundamental constraints on Pb mobility mechanisms as well as valuable information on the thermal evolution of the mineral. The ability for APM to characterise the distribution of trace elements and isotopic compositions at the nanoscale provides a highly effective way to test between the two proposed models for common Pb incorporation into titanite.

Two coeval titanite grains were chosen, from previously dated sample 570128 (Kirkland et al., 2017) for detailed examination in order to help resolve which of the two contrasting processes for common Pb incorporation occurred. Titanite from this specific sample yields a best estimate for crystallization of 1762 ± 11 Ma (Kirkland et al., 2017) (Fig. 2). Grains were selected with vastly contrasting common Pb contents. Grain 1 (original analysis i.d. 31) is near concordant and apparently dominated by radiogenic Pb. Grain 2 (original analysis i.d. 8) indicates a very high calculated common Pb content (F207% = 85).

3. Analytical methodology

Fist-sized blocks of amphibolite were disaggregated by an electric selective fragmentation system (SelFrag), using a high voltage electrodynamic discharge. The disaggregated rock was elutriated, dried, magnetically and density separated. Density separation used sodium polytungstate. The resultant heavy fraction was mounted in epoxy resin and polished to half grain thickness. The grain mount was polished with 0.06 μm colloidal silica in pH 10 NaOH solution. The polished mount

was coated with a thin layer of carbon to limit charging in the scanning electron microscope (SEM). Titanite was identified in the mounts using a TESCAN Integrated Mineral Analyser and dated using LA-ICPMS which has been previously reported (Kirkland et al., 2017).

3.1. Microstructural analysis by scanning electron microscopy

All SEM imaging and analyses were conducted on a Tescan MIRA3 Field Emission SEM, housed in the Microscopy & Microanalysis Facility (John de Laeter Centre) at Curtin University, Perth, Western Australia. Backscattered secondary electron (BSE) imaging was acquired at 20 kV accelerating voltage using a retractable dual scintillator (YAG) BSE detector. The image brightness and contrast was optimised prior to collection to qualitatively reveal the internal growth and deformation features of the titanite grains.

EBSD data were acquired using the automatic mapping capability of Oxford Instruments AZtec 2.3 software coupled with a NordlysNano EBSD detector. EBSD patterns were collected from each node of a user-defined grid, with grid nodes spaced at 1 μm in both x and y directions. Empirically collected patterns were indexed against theoretical diffraction patterns, derived from the crystallography data of a natural titanite sample (E2312) by Hawthorne et al. (1991), using the 8–10 strongest lattice planes in the empirically obtained pattern. The quality of indexing was good, as seen in mean angular deviations of ~0.5°. Full grain maps, collected at a 1 μm step size, for grains 1 and 2 represent the analysis of ~87,000 and ~90,000 EBSD patterns respectively.

All EBSD data were post-processed using Oxford Instruments Channel 5.12 software to remove 'wildspikes' and interpolate non-indexed points using a 6 nearest neighbour filter following standard procedures (Reddy and Hough, 2013). Orientation maps were produced using the Channel 5 'texture' component in which each pixel was coloured for minimum misorientation relative to a user-defined reference orientation. EBSD maps were constructed to show orientation variations within the grains and highlight the location of low- and high-angle boundaries.

3.2. Atom probe specimen preparation

To investigate Pb distribution in these grains, six atom probe needles were prepared (Fig. 3): two from Grain 1 (specimen 1 and 2) and four from Grain 2 (specimen 3 to 6). Atom probe specimens were specifically targeted based on the microstructural data obtained by EBSD. Hence, specimen 1 targeted a low-angle boundary (5° misorientation) in grain 1, whereas specimen 2 was prepared from an undeformed domain of the same grain. Specimen 3 to 6 targeted undeformed areas of grain 2.

The needle shaped specimens needed for APM analyses were prepared on a Tescan Lyra3 Ga$^+$ Focused Ion Beam SEM (FIB-SEM), which form part of National Resource Sciences Precinct's Advanced Resource Characterisation Facility (ARCF) and is housed in the John de Laeter Centre (JdLC), Curtin University. Specimen preparation followed the lift-out method typically used for non-conducting materials (Thompson et al., 2007). The FIB-SEM was operated at an accelerating voltage of 30 kV during coarse milling and specimen sharpening with a final polishing stage, to remove the surface layer affected by high energy Ga implantation, being carried out at 2 kV accelerating voltage. Details about the sample preparation specific to this instrument are given elsewhere (Fougerouse et al., 2016a; Peterman et al., 2016).

3.3. Atom probe analysis of titanite

For non-conducting material such as titanite, APM uses a pulsed laser to evaporate atomic and molecular species from a needle shape specimen to which a high electric field has been applied (Larson et al.,
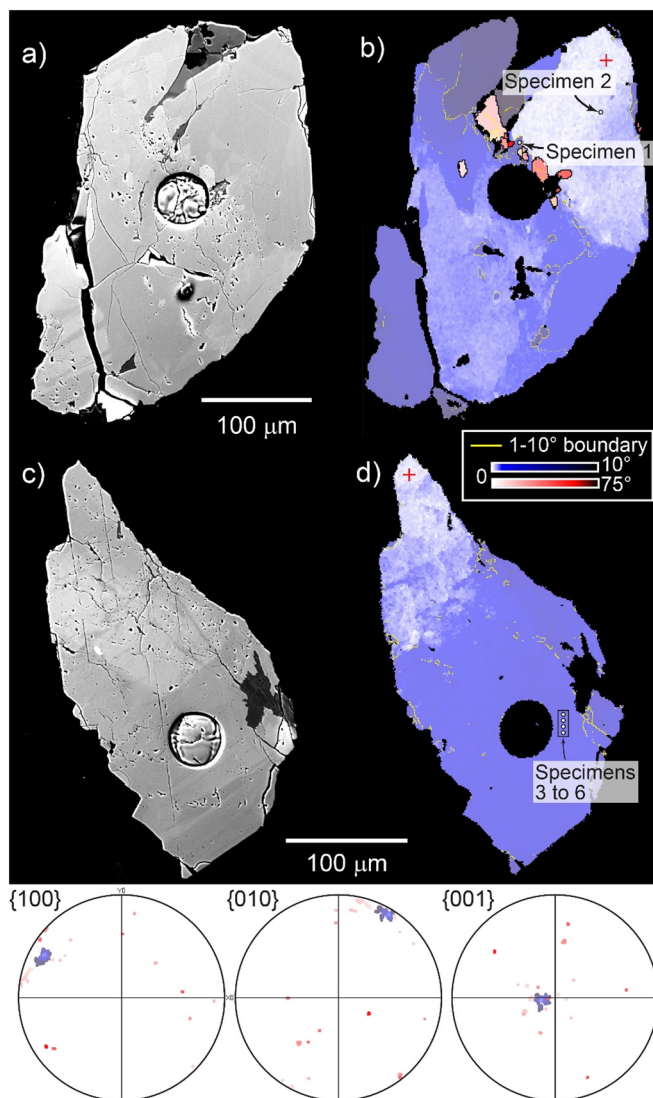

Fig. 3. (A, C) Backscattered electron and (B, D) electron backscattered diffraction images of grains 1 and 2. The location of specimens 1, 2 (Grain 1), 3, 4, 5, and 6 (Grain 2) are denoted by circles. Grain misorientation relative to the red cross hairs. (Bottom) Equal area, lower hemisphere pole figures of 43,028 EBSD orientation data points for titanite grain 1. (For interpretation of the references to colour in this figure legend, the reader is referred to the web version of this article.)

2013). Following evaporation, atoms and molecular species are ionised and accelerated by the electric field to hit a position sensitive detector. The sequence and position of detector hits allow the positioning of the ionic or molecular species to be reconstructed in 3D and the timing between the laser pulse and detector hit allow ionic species to be identified by time-of-flight mass spectrometry. APM analyses were conducted on a Cameca LEAP4000X HR at the Geoscience Atom Probe Facility, part of the ARCF and housed at the JdLC, Curtin University. The instrument was operated in laser mode with a UV laser (λ = 355 nm), laser pulse energy of 300 pJ and pulse frequency of 200 kHz. The specimens were maintained at a temperature of 60 K and the automated detection rate was set at 0.01 atoms/pulse. In the mass-to-charge spectrum, peaks twice above the background were ranged using IVAS 3.6.14 software. The 3D position of the ionic species was reconstructed using the voltage curve to model the evolution of the tip-radius during each experiment. More experiment details can be found in Supplementary Table 1 following recommendations of Blum et al. (2017).

4. Results

4.1. Microstructural analysis of titanite

Backscattered electron (BSE) imaging of Grain 1 reveals subtle, but complex, compositional features that appear to be related to growth and/or recrystallization of the titanite. Some greyscale variations through Grain 1 (Fig. 3a) coincide with orientation microstructure observed in the EBSD data (Fig. 3b), indicating that a component of the backscatter signal is orientation dependent. The grain contains small voids and fractures that define a discontinuous planar feature.

EBSD orientation maps of Grain 1 reveal low- and high-angle boundaries with the magnitude of the misorientation angle between the host titanite and new-grains being as large as 75°. However, the microstructure is heterogeneously developed with the host grain only accommodating ~8° of misorientation across this grain. In contrast, new-grains and low-angle boundaries define a zone of localised deformation and recrystallization that extends almost across the whole grain (Fig. 3b). Crystallographic orientation variations across low-angle boundaries are generally consistent with the operation of crystal plasticity by a subgrain-rotation recrystallization mechanism. In contrast, the magnitude of misorientations across the high angle boundaries, and the absence of systematic, rational, lattice misorientations between host and new-grains (Fig. 3), support the formation of new-grains by nucleation at low-angle boundary sites followed by growth through a grain boundary migration mechanism. A similar new-grain growth process has been reported in monazite (e.g. Erickson et al., 2015).

Grain 2 reveals sector zonation under BSE (Fig. 3c). Grain 2 differs from Grain 1 in that it has significantly fewer low-angle boundaries and none of the high-angle boundaries (Fig. 3d). Grain 2 records minor lattice distortion with a maximum misorientation of ~5°, with much of the grain showing < 1° of lattice misorientation. EBSD data therefore indicate little deformation or microstructural complexity across Grain 2.

4.2. Geochemistry

The composition of this titanite has been previously reported (Kirkland et al., 2017) but it is relevant to the discussion of common Pb content and hence is explored with specific reference to that in this contribution (Supplementary Table 2). Analyses of the NIST612 glass standard obtained during the titanite LA-ICPMS analytical session are provided in Supplementary Table 3. Plots of total Pb versus U concentration reveal a broadly coupled relationship, where greater U is typically associated with greater total Pb concentration (Fig. 4). However, those analyses with high F207% are distinct from this pattern and are associated with low U and very high total Pb concentrations. Time correction for U and Pb concentrations does not alter this relationship. High F207% is also associated with low total REE content and La_N/Sm_N ratios closer to unity (Fig. 2). Elevated F207% is also associated with very low Th content. F207% is calculated by the following procedure: The 207 corrected age is recast as a concordant $^{206}Pb/^{238}U$ ratio where the 207 corrected age is based on the preferred common Pb composition as discussed in detail in Kirkland et al. (2017) e.g. $^{207}Pb/^{206}Pb = 0.78$.

Fig. 4. Plot of total Pb (ppm) versus U (ppm) concentration with data point circles scaled and coloured for F207%. Many grains are nearly concordant (see Fig. 2), i.e., they have little % of common Pb, so total Pb (most of which is radiogenic) scales linearly with U. However, those analyses with anomalously high F207% have low U and high Pb concentrations.

spectra are typically complex, compared to materials traditionally analysed by atom probe, with peaks corresponding to elemental and molecular species that are singularly to triply charged. Trace elements in the titanite are commonly evaporated as elemental species (e.g. Mg, Al, K & Pb), though the major peaks for iron are found as molecular FeO^+. Lead in the mass spectra was identified at 103 Da for $^{206}Pb^{++}$. A peak overlap between $^{207}Pb^{++}$, $^{208}Pb^{++}$ and a broad $Si_2O_3^+$ peak precluded the measurement of these Pb isotopes. This interference between Pb^{++} and $Si_2O_3^+$ has been observed in other silicates such as zircons (Valley et al., 2014; Peterman et al., 2016) and can be minimised by selection of suitable acquisition conditions, though not entirely eliminated (Saxey et al., 2018). No peak could be identified above the background for ^{204}Pb and was therefore not quantified in this study. As a result, the Pb distribution reported is based on the quantification of $^{206}Pb^{++}$ only. No peak could be identified for U in any of the specimen datasets. Peaks previously reported for ^{238}U in baddeleyite and zircon at 135, 270, 84.66 and 127 Da for $^{238}U^{16}O_2^{++}$, $^{238}U^{16}O^{++}$, $^{238}U^{16}O^{+++}$ and $^{238}U^{16}O^{++}$, respectively (White et al., 2017; Piazolo et al., 2016) were not present in the titanite spectrum (Fig. 5). Thus in this work atom probe tomography is imaging initial Pb, Pb derived from radiogenic production, and Pb from migration if it occurred.

The low-angle boundary from Grain 1 appears in the atom probe reconstruction as a planar domain oblique to the needle specimen axis (Fig. 6). This domain is composed of an array of tubular linear features, flattened in the low-angle boundary plane, with the spacing between adjacent features being ~10 nm (Fig. 6). Relative to the main part of the specimen, these features are enriched in Al, Fe, Mg, and K (Fig. 6),

$$\text{Concordant}^{206}Pb/^{238}U \text{ ratio} = \text{EXP}(0.000155125 \times {}^{207}\text{corrected}^{238}U/^{206}Pb \text{ age}) - 1$$

$$F207\% = 100 \times (1 - \text{Concordant}^{206}Pb/^{238}U \text{ ratio}/^{206}Pb/^{238}U \text{ measured})$$

4.3. Nanoscale chemical distribution

The six atom probe specimens yielded between 23 and 83 million atomic species. Mass-to-charge ratio spectra for each of these tips are broadly similar and a representative spectrum is given in Fig. 5. The
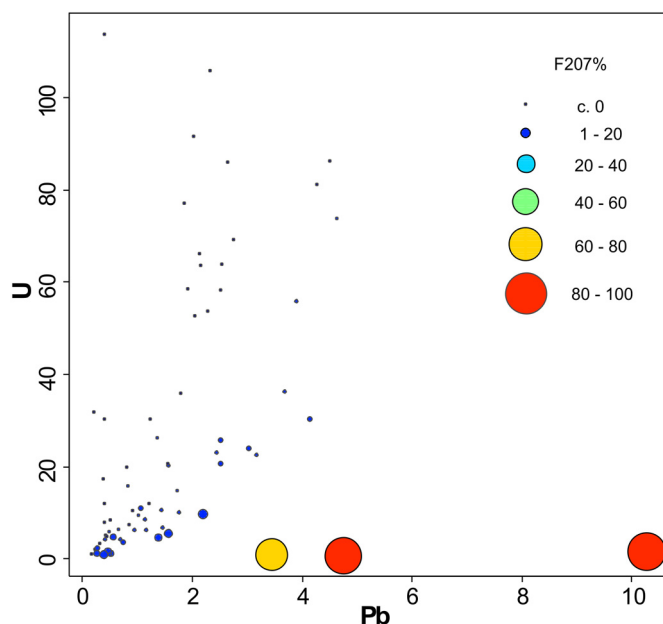
but the extent of the enrichment is relatively small with an increase of ~3 at.% for Al and Fe (Fig. 7). The trace element enrichment in the features is accommodated by a depletion in Ca and Ti. In contrast to the enriched trace elements, the distribution of Pb throughout the atom probe specimen is homogeneous with no change in composition being
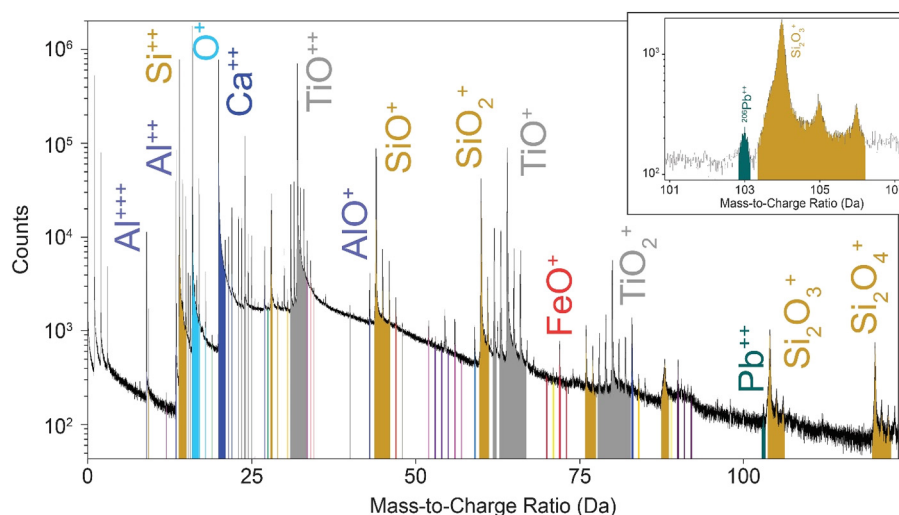
Fig. 5. Representative atom probe mass-to-charge ratio spectrum acquired from the tip of titanite specimen 1. Species are ranged and identified by their mass-to-charge ratio. Insert: Close up of the mass spectrum for 101 to 107 Da. $^{206}Pb^{++}$ is clearly distinct from a $Si_2O_3^+$ molecular species that overlaps $^{207}Pb^{++}$ and $^{208}Pb^{++}$ and makes these isotopes unquantifiable.

observed in the low-angle boundary (Fig. 6).

The atom probe data of specimen 2, Grain 1, revealed a homogeneous distribution of all ranged species throughout the entire specimen. All four specimens from Grain 2 also provided homogeneous distributions of trace and major elements including Al, Fe, K, Mg and Pb (Figs. 8 and S1).

5. Discussion

5.1. Trace element mobility in titanite

Microstructural analysis of titanite from amphibolites in the Karrat Group, Rae Craton, reveals heterogeneous strain at the grain-scale and localised domains of lattice distortion and recrystallisation, consistent with heterogeneous deformation of the titanite at an intragrain scale. Within low-angle boundaries, specifically targeted for APM and formed by sub-grain rotation recrystallisation, there is an enrichment in trace amounts of Mg, Al, K and Fe. This enrichment is manifest in linear features, which are consistently oriented in the low-angle boundary plane. We interpret these features to represent an interface dislocation network that is decorated by the trace elements. Similar features have previously been reported in atom probe studies of zircon (Piazolo et al., 2016). The observed enrichment of trace elements, such as Mg, Al, K and Fe, in dislocations may reflect the migration of interstitial ions into the region around the dislocation, driven by the elastic strain energy around the dislocation, and the subsequent migration of the dislocation to the low-angle boundary (Cottrell and Bilby, 1949). Such a mechanism is most likely to affect the smaller ions (Mg, Al and Fe). Alternatively, the enrichment may represent the migration of externally-derived trace elements along the interface dislocation network subsequent to boundary generation (Joesten, 1991; Plümper et al., 2012; Fougerouse et al., 2016b).

Our data does not allow us to unequivocally discriminate between the potential mechanisms responsible for the trace element segregation. Nonetheless, K^+ is highly incompatible in the titanite crystal structure (Prowatke and Klemme, 2005; Tiepolo et al., 2002) and is a large cation (K+ ionic radius = 0.133 nm) which is energetically unlikely to migrate to the region of elastic strain around a dislocation (Cottrell and Bilby, 1949; Shannon, 1976). With an ionic radius of 0.119 nm, Pb^{2+} is only slightly smaller than K^+ and the absence of Pb segregation in the dislocation network therefore supports the interpretation that K segregation does not reflect a Cottrell atmosphere process. Additionally, K, Mg, Fe and Al are all present in abundance in the host rock, where chlorites surround the titanite crystals, suggesting that these elements

may be externally derived during or after deformation.

The atom probe data did not resolve any Pb enrichment in the investigated low-angle boundary nor elsewhere. Previous study of a deformed zircon revealed the absence of Pb segregated in dislocations decorated with Al and Y (Piazolo et al., 2016). Those authors preferred model was that Pb was trapped in Cottrell atmospheres during dislocation creep and was subsequently diffused out of the low-angle boundary by pipe diffusion (Piazolo et al., 2016). However, in the case of Grain 1 titanite, our LA-ICPMS analysis spot, located on the edge of a zone of deformation crossing the grain, is apparently concordant and no significant radiogenic-Pb loss appears to have occurred during deformation as its 207 corrected age of 1698 ± 36 Ma is similar to the best estimate age of 1762 ± 11 Ma. This concordance implies that Pb is not affected by dislocation migration in titanite and suggests that Pb^{++} ions may be too large to fit in the Cottrell atmosphere catchment zone for a dislocation in the titanite lattice.

The absence of Pb enrichment in the dislocations, above background, also suggests that common Pb did not ingress along the deformation microstructure network. Furthermore, the LA-ICPMS data indicates that the deformed grain (Grain 1) has lower estimated common Pb than other grains lacking this structural complexity (Kirkland et al., 2017).

5.2. A model for common Pb incorporation in titanite

Given that no evidence of a Pb transportation network has been imaged on the nanoscale, a viable alternative to derive low common $^{207}Pb/^{206}Pb$ ratios is mixing of regional precursor Pb sources at or prior to crystallization (Fig. 9). One common Pb source for this titanite was likely generated through radiogenic production, in primary U-bearing minerals, that recrystallized during metamorphism of this rock, in order to result in the sub 0.8 $^{207}Pb/^{206}Pb_c$ ratio.

Grain 2 with homogeneous BSE, EBSD and atomic distribution is estimated to contain 85% common Pb yet there are no imaged transport pathways viable to move Pb into this grain. Furthermore, the time-temperature path of this rock after titanite crystallization is inconsistent with Pb diffusion processes (Kirkland et al., 2017). Rather, the elevated common Pb cargo of this grain must be a primary crystallization-related feature, with Pb becoming bound into the developing titanite crystal lattice.

Although a regression through all 570,128 analyses indicates scatter in excess of analytical uncertainties alone, a consistent $^{207}Pb/^{206}Pb_c$ ratio is nonetheless implied as comparable Pb compositions are regionally ubiquitous from titanite in this unit (Kirkland et al., 2017).

Specimen 1: Low common Pb - low-angle boundary
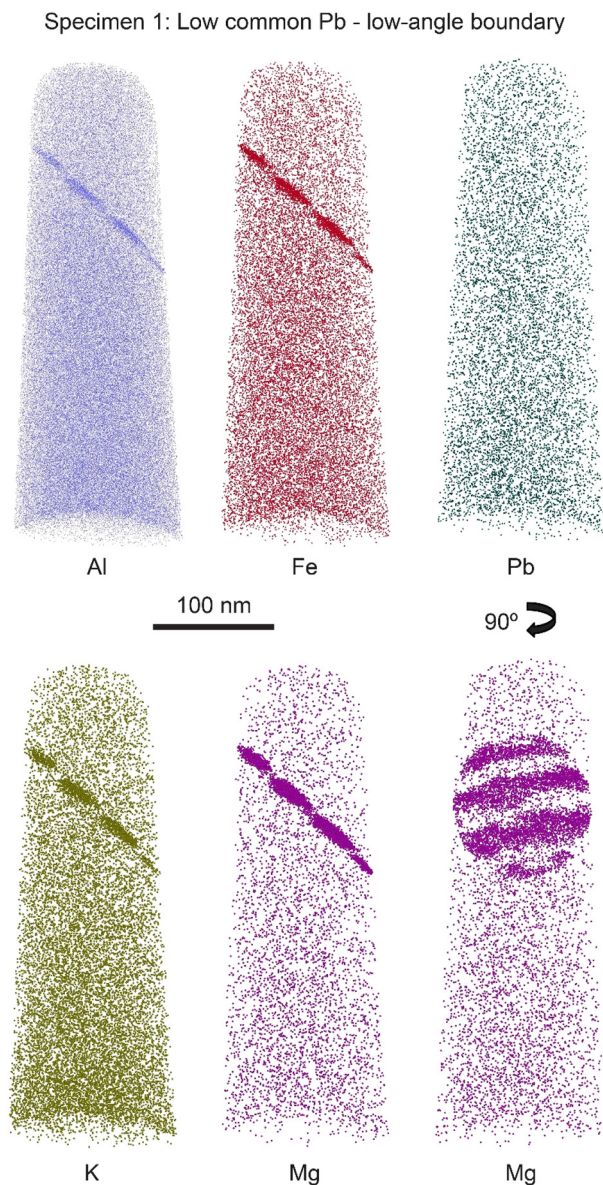

Al Fe Pb

100 nm 90°

K Mg Mg

Fig. 6. Atom probe tomographic reconstruction of specimen 1, Grain 1. The enrichment in Al, Fe, K and Mg is spatially associated with a low angle boundary in the grain. The discontinuous nature of the enrichment and the lack of depletion halo is consistent with lattice dislocations controlling element mobility. The Pb concentration appears homogeneous across the needle.

Moreover, a subset of the least radiogenic analyses from 570,128, which appear distinct in $^{207}Pb/^{206}Pb$ space, define an identical upper intercept within uncertainty to all other titanite datasets from the Karrat Group ($^{207}Pb/^{206}Pb_c = 0.780 \pm 0.071$). The excess scatter also appears unlikely to have originated from prolonged titanite growth as best age estimates on titanite in this unit are identical within uncertainty (Kirkland et al., 2017). Furthermore, no correlation between U and 207 corrected age is apparent as might be expected for pervasive radiation driven radiogenic Pb loss causing the scatter. The excess scatter in 570,128 may be due to minor Pb loss, inheritance of radiogenic Pb that remains undiagnosed in atom probe tomography, or minor underestimation of analytical uncertainties. In any case, two observations on the nature of the common Pb content of this titanite appear pertinent with regard to the process by which titanite incorporates its initial Pb cargo. Firstly, the isotopic composition of common Pb in this titanite population, at least in terms of $^{207}Pb/^{206}Pb_c$, is similar. Secondly, the amount of common Pb is highly variable.
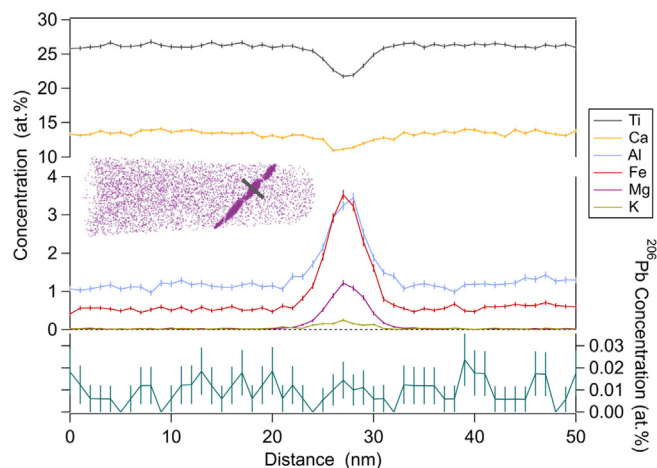

Fig. 7. One-dimensional concentration profile across a low angle boundary in specimen 1, showing increased Al, Fe, Mg and K in the dislocation, but no enrichment in Pb. Inset image shows a Mg atom map with the location and size of the 50 nm profile. Indicated uncertainties are 1-sigma, based on the counts for each data point. The Pb profile is dominated by background noise in the mass spectrum.
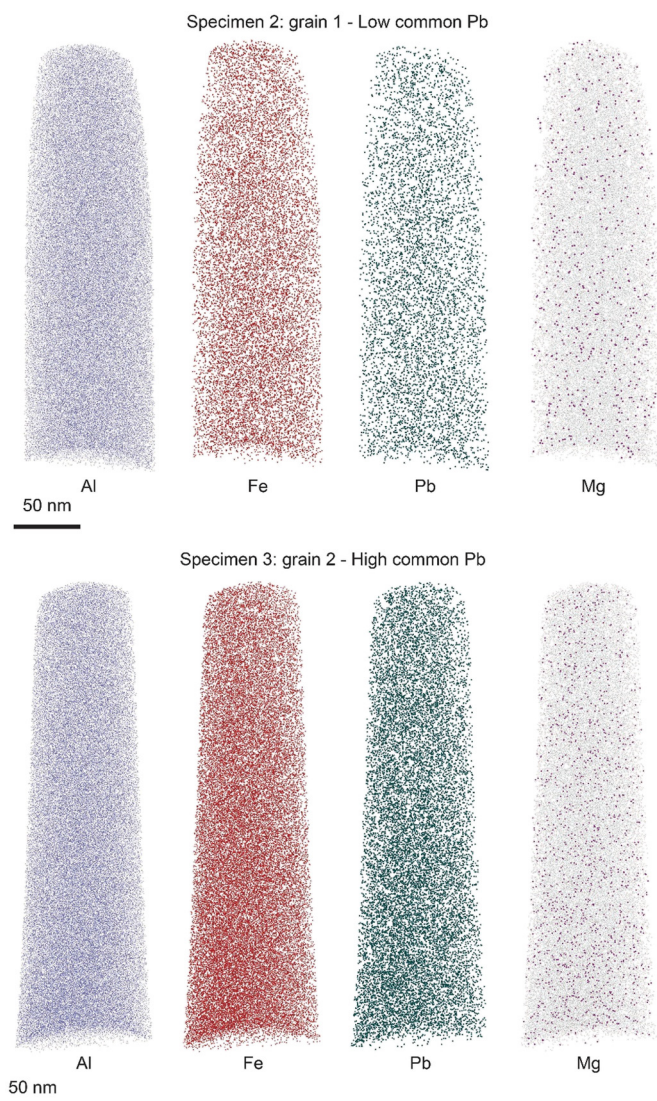
Specimen 2: grain 1 - Low common Pb

Al Fe Pb Mg

50 nm

Specimen 3: grain 2 - High common Pb

Al Fe Pb Mg

50 nm

Fig. 8. Atom probe tomographic reconstruction of specimen 2, Grain 1 and specimen 3, Grain 2. A homogeneous distribution of elements is indicated throughout even though Grain 1 indicates low common Pb and Grain 2 extreme common Pb.
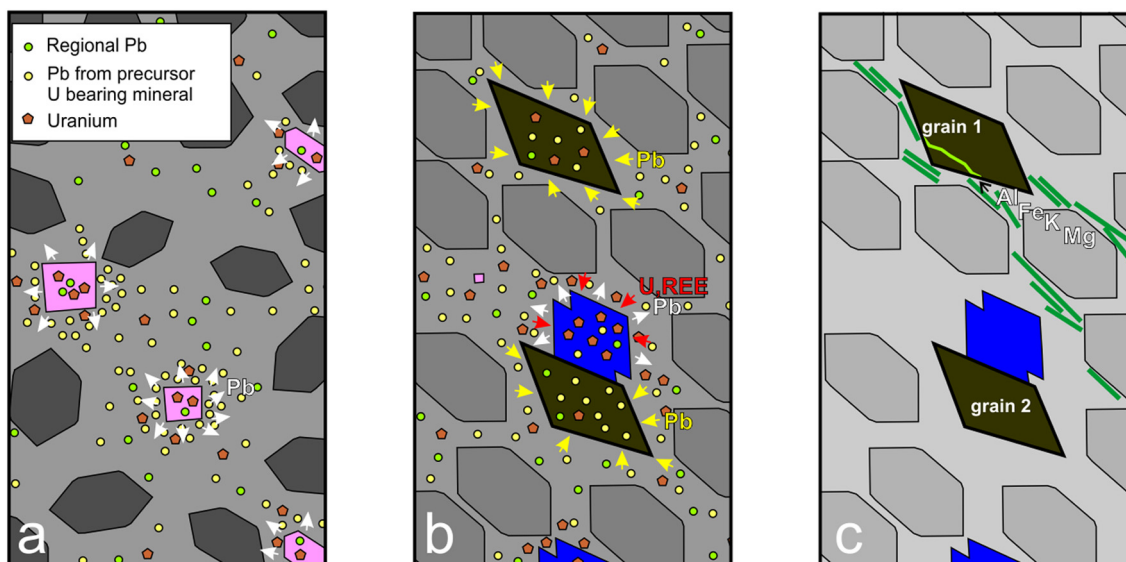
Fig. 9. Schematic cartoon for a model for the development and modification of titanite (brown) in the Karrat Group. A; Precursor U bearing phases (pink) undergo recrystallization at or prior to 1770 Ma metamorphism. Radiogenic-Pb from these precursor U bearing minerals is released into the metamorphic reservoir where it is homogenised along with other regional sources of Pb. B; During 1770 metamorphism titanite grows in the regional D2 fabric. Titanite growing in competition with a phase that excludes Pb, but acquires REE and U (blue), accommodates greater Pb into its structure. In contrast titanite without the influence of this competing phase acquires relatively more U and REE and proportionally less common Pb. C; During later chlorite (green) related alteration titanite is weakly deformed and Al, Mg, K and Fe from the grain edges is swept through the titanite by dislocation migration along a low angle boundary, but Pb is immobile. (For interpretation of the references to colour in this figure legend, the reader is referred to the web version of this article.)

The similarity in $^{207}Pb/^{206}Pb_c$ suggests a homogenised metamorphic Pb reservoir from which the titanite grew, yet the variability in non-radiogenic quantity suggests a process where Pb was accommodated to variable degrees into the crystal structure. A process where simply little radiogenic-Pb was produced from little U, is not consistent with the inverse correlation of U and Pb concentration. This holds even after considering radioactive production of Pb from U. Rather, a differential uptake of Pb, as the principal cause of variation in the amount of common Pb, is supported by the relationship between REE's and U in the different titanite grains (Fig. 2). Specifically, those analyses that have high F207%, have elevated total Pb, at low U concentration, whereas the remaining population have little common Pb, plot at the radiogenic end of the mixing line, and have broadly coupled Pb and U concentrations. When common Pb is high the amount of REE is reduced and the REE profile, especially for the LREE, is flattened. Flattening of the REE profile correlates with a reduction in U and Th, whilst increase in total Pb concentration (and common Pb) is consistent with competition from other metamorphic minerals growing along with the titanite. A mineral that accommodated U, Th and LREEs to leave a residual local reservoir enriched in Pb is indicated by the chemical relationships between high and low common Pb titanite components. Titanite grown during metamorphism synchronously as a mineral or minerals incorporating U, Th and LREE would be depleted in these elements, yet become enriched in Pb. Hence, the common Pb value recorded within a titanite grain holds information useful to distinguish its growth history. For example, titanite with ancient common Pb can be contrasted against grains with much lower $^{207}Pb/^{206}Pb_c$, with the later indicating recrystallization of a radiogenic Pb-bearing phase during metamorphic genesis.

These findings have clear implications for the most appropriate choice of common Pb correction strategy; titanite common Pb appears governed by its growth environment not the later ingress of Pb. The proposed origin for a relatively radiogenic common Pb composition in metamorphic titanite, derived from breakdown of U-rich minerals, implies that use of low-U phases, like feldspar, to determine the common Pb composition of metamorphic titanite is potentially unreliable unless no recrystallization, specifically of U bearing minerals, can be unequivocally demonstrated. The apparently uniform common Pb composition, but highly variable common Pb amount, in many titanite populations favours a regression-based calculation approach whose

goodness of fit provides a measure of confidence in common Pb composition and radiogenic component age where scatter in the regression may imply heterogeneous common Pb component, prolonged titanite growth or different Pb blocking temperatures on an inter grain scale. Furthermore, it is important to note that a ^{204}Pb based correction will make an assumption on the composition of common Pb which in the case of recrystallization will likely be dramatically different from regional Pb models, due to break-down of radiogenic-Pb bearing phases, with deleterious effects on calculated ages.

6. Conclusions

The common Pb isotopic composition is similar throughout a population of metamorphic titanite in a Greenland amphibolite. This common Pb composition is distinctly different to regional Pb models and implies the break-down of precursor U bearing phases to produce a homogeneous Pb reservoir from which metamorphic titanite grew. Common Pb was incorporated into titanite during its growth and not during later deformation related processes as no Pb is imaged along deformation microstructures. Although some elements appear to be segregated in dislocations, Pb distribution was not affected by the migration of dislocations, being either too large to fit within the distorted lattice or not present outside the grain to be ingressed through the crystal. A grain with extreme common Pb shows little lattice misorientation and no obvious deformation microstructures and reveals a homogeneous distribution of elements on the atomic scale. Such homogeneous distribution of Pb is consistent with common Pb being bound within the crystal during growth, not introduced by more recent processes. Also, for a high F207% titanite population, the Pb distribution cannot be a function of radiogenic in-growth as these grains have low U concentration yet have the highest total Pb content. The low total REE and La_N/Sm_N – near unity for high F207% analyses – imply a mineral-driven element partitioning process in the metamorphic reservoir that titanite grew from. The chemical composition of common Pb rich titanite, which is low in U, Th and LREE, implies a growth-related partitioning process during metamorphism where titanite was starved of U, Th and LREE, yet enriched in Pb from an isotopically homogeneous (in terms of $^{207}Pb/^{206}Pb_c$) metamorphic fluid. Our approach illustrates that the correct choice of common Pb correction

strategy for titanite may not be straightforward. However, compositional information at nanoscale can successfully refine this strategy.

Supplementary data to this article can be found online at https://doi.org/10.1016/j.chemgeo.2018.03.026.

Acknowledgments

References

Aleinikoff, J.N., Wintsch, R.P., Fanning, C.M., Dorais, M.J., 2002. U–Pb geochronology of zircon and polygenetic titanite from the Glastonbury Complex, Connecticut, USA: an integrated SEM, EMPA, TIMS, and SHRIMP study. Chem. Geol. 188 (1), 125–147.

Blum, T.B., Darling, J.R., Kelly, T.F., Larson, D.J., Moser, D.E., Perez-Huerta, A., Prosa, T.J., Reddy, S.M., Reinhard, D.A., Saxey, D.W., Ulfig, R.M., Valley, J.M., 2017. Best practices for reporting atom probe analysis of geological materials. In: Moser, D.E., Corfu, F., Darling, J.R., Reddy, S.M., Tait, K. (Eds.), Microstructural Geochronology: Planetary Records Down to Atom Scale. vol. 232. AGU Geophysical Monograph, pp. 369–373.

Chew, D.M., Petrus, J.A., Kamber, B.S., 2014. U–Pb LA–ICPMS dating using accessory mineral standards with variable common Pb. Chem. Geol. 363, 185–199.

Connelly, J.N., Thrane, K., 2005. Rapid determination of Pb isotopes to define Precambrian allochthonous domains: an example from West Greenland. Geology 33, 953–956.

Cottrell, A.H., Bilby, B., 1949. Dislocation theory of yielding and strain ageing of iron. Proc. Phys. Soc. London, Sect. A 62 (1), 49.

Erickson, T.M., Pearce, M.A., Taylor, R.J.M., Timms, N.E., Clark, C., Reddy, S.M., Buick, I.S., 2015. Deformed monazite yields high-temperature tectonic ages. Geology 43 (5), 383–386.

Escher, A., Pulvertaft, T.C.R., 1976. Rinkian mobile belt of West Greenland. In: Escher, A., Watt, W.S. (Eds.), Geology of Greenland. Geological Survey of Greenland, Copenhagen, pp. 105–119.

Fougerouse, D., Reddy, S.M., Saxey, D.W., Rickard, W.D., Van Riessen, A., Micklethwaite, S., 2016a. Nanoscale gold clusters in arsenopyrite controlled by growth rate not concentration: evidence from atom probe microscopy. Am. Mineral. 101 (8), 1916–1919.

Fougerouse, D., Micklethwaite, S., Halfpenny, A., Reddy, S.M., Cliff, J.B., Martin, L.A., Kilburn, M., Guagliardo, P., Ulrich, S., 2016b. The golden ark: arsenopyrite crystal plasticity and the retention of gold through high strain and metamorphism. Terra Nova 28 (3), 181–187.

Garde, A.A., 1978. The lower Proterozoic Maarmorilik formation east of Mârmorilik, West Greenland. Medd. Grønland 200, 1–71.

Gibson, G.M., Ireland, T.R., 1996. Extension of Delamerian (Ross) orogen into western New Zealand: Evidence from zircon ages and implications for crustal growth along the Pacific margin of Gondwana. Geology 24 (12), 1087–1090.

Grocott, J., McCaffrey, K.J.W., 2017. Basin evolution and destruction in an Early Proterozoic continental margin: the Rinkian fold–thrust belt of central West Greenland. J. Geol. Soc. 174 (3), 453–467.

Grocott, J., Vissers, R.L.M., 1984. Field mapping of the early Proterozoic Karrat Group on Svartenhuk Halvø, central West Greenland. In: Geological Survey of Greenland Report, 120, pp. 25–31.

Hawthorne, F.C., Groat, L.A., Raudsepp, M., Ball, N.A., Kimata, M., Spike, F.D., Gaba, R., Halden, N.M., Lumpkin, G.R., Ewing, R.C., Greegor, R.B., Lytle, F.W., Ercit, T.S., Rossman, G.R., Wicks, F.J., Ramik, R.A., Sherriff, B.L., Fleet, M.E., McCammon, C.A., 1991. Alpha-decay damage in titanite. Am. Mineral. 76, 370–396.

Henderson, G., 1969. The use of structural contour maps in the study of gneiss– metasediment relations in the Umanak area, West Greenland. In: WynneEdwards, H.R. (Ed.), Age Relations in High-grade Metamorphic Terrains. vol. 5. Geological Association of Canada, Special Paper, pp. 129–142.

Henderson, G., Pulvertaft, T.C.R., 1967. The stratigraphy and structure of the Precambrian rocks of the Umanak area, West Greenland. In: Meddelelser fra Dansk Geologisk Forening. vol. 17. pp. 1–20.

Henderson, G., Pulvertaft, T.C.R., 1987. The lithostratigraphy and structure of a Lower Proterozoic dome and nappe complex. In: Geological Survey of Greenland Descriptive text for Geological Map of Greenland 1:100 000-scale Sheets Mârmorilik 71V.2 Syd, Nûgâtsiaq 71V.2 Nord, Pangnertôq 72V.2 Syd. Grønlands geologiske Undersøgelse, Copenhagen.

Hoffman, P.F., 1990. Dynamics of the tectonic assembly of north-east Laurentia in geon 1.8 (1.9–1.8 Ga). Geosci. Can. 17, 222–226.

Horstwood, M.S.A., Foster, G.L., Parrish, R.R., Noble, S.R., Nowell, G.M., 2003. Common-Pb corrected in situ U–Pb accessory mineral geochronology by LA-MC-ICP-MS. J. Anal. At. Spectrom. 18, 837–846.

Joesten, R., 1991. Grain-boundary diffusion kinetics in silicate and oxide minerals. In: Ganguly, J. (Ed.), Diffusion, Atomic Ordering, and Mass Transport. Advances in Physical Geochemistry. vol. 8. Springer, New York, NY, pp. 345–395.

Kirkland, C.L., Hollis, J., Danišík, M., Petersen, J., Evans, N.J., McDonald, B.J., 2017. Apatite and titanite from the Karrat Group, Greenland; implications for charting the thermal evolution of crust from the U-Pb geochronology of common Pb bearing phases. Precambrian Res. 300, 107–120.

Kramers, J., Frei, R., Newville, M., Kober, B., Villa, I., 2009. On the valency state of radiogenic lead in zircon and its consequences. Chem. Geol. 261, 4–11.

Larson, D.J., Prosa, T.J., Ulfig, R.M., Geiser, B.P., Kelly, T.F., 2013. Local Electrode Atom Probe Tomography: A User's Guide. ISBN 1-4614-8721-0_1. Springer Science +Business Media, New York.

Marsh, J.H., Smye, A.J., 2017. U-Pb systematics and trace element characteristics in titanite from a high-pressure mafic granulite. Chem. Geol. 466 (Supplement C), 403–416.

Peterman, E.M., Reddy, S.M., Saxey, D.W., Snoeyenbos, D.R., Rickard, W.D., Fougerouse, D., Kylander-Clark, A.R., 2016. Nanogeochronology of discordant zircon measured by atom probe microscopy of Pb-enriched dislocation loops. Sci. Adv. 2 (9), e1601318.

Piazolo, S., La Fontaine, A., Trimby, P., Harley, S., Yang, L., Armstrong, R., Cairney, J.M., 2016. Deformation-induced trace element redistribution in zircon revealed using atom probe tomography. Nat. Commun. 7.

Plümper, O., King, H.E., Vollmer, C., Ramasse, Q., Jung, H., Austrheim, H., 2012. The legacy of crystal-plastic deformation in olivine: high-diffusivity pathways during serpentinization. Contrib. Mineral. Petrol. 163 (4), 701–724.

Prowatke, S., Klemme, S., 2005. Effect of melt composition on the partitioning of trace elements between titanite and silicate melt. Geochim. Cosmochim. Acta 69 (3), 695–709.

Pulvertaft, T.C.R., 1973. Recumbent folding and flat-lying structure in the Precambrian of northern West Greenland. Philos. Trans. R. Soc. Lond. Ser. A 273, 535–545.

Reddy, S.M., Hough, R.M., 2013. Microstructural evolution and trace element mobility in Witwatersrand pyrite. Contrib. Mineral. Petrol. 166, 1269–1284.

Reddy, S.M., van Riessen, A., Saxey, D.W., Johnson, T., Rickard, W., Fougerouse, D., Fischer, S., Prosa, T., Rice, K., Reinhard, D., Chen, Y., Olson, D., 2016. Mechanisms of deformation-induced trace element migration in zircon resolved by atom probe and correlative microscopy. Geochim. Cosmochim. Acta 195, 158–170.

Romer, R.L., 2001. Lead incorporation during crystal growth and the misinterpretation of geochronological data from low-^{238}U/^{204}Pb metamorphic minerals. Terra Nova 13, 258–263.

Romer, R.L., Rötzler, J., 2003. Effect of metamorphic reaction history on the U-Pb dating of titanite. In: Vance, D., Müller, W., Villa, I.M. (Eds.), Geochronology: Linking the Isotopic Record with Petrology and Textures. vol. 220. Geological Society, London, Special Publication, pp. 147–158.

Romer, R.L., Siegesmund, S., 2003. Why allanite may swindle about its true age. Contrib. Mineral. Petrol. 146, 297–307.

Sanborn-Barrie, M., Thrane, K., Wodicka, N., Rayner, N., 2017. The Laurentia – West Greenland connection at 1.9 Ga: new insights from the Rinkian fold belt. Gondwana Res. 51, 289–309.

Saxey, D., Reddy, S.M., Fougerouse, D., Rickard, W.D., 2018. The Optimization of Zircon Analyses by Laser-assisted Atom Probe Microscopy: Insights from the 91500 Zircon Standard. Microstructural Geochronology: Planetary Records Down to Atom Scale. pp. 293–313.

Shannon, R.D., 1976. Revised effective ionic radii and systematic studies of interatomic distances in halides and chalcogenides. Acta Crystallogr. Sect. A: Cryst. Phys., Diffr., Theor. Gen. Crystallogr. 32 (5), 751–767.

Stacey, J.S., Kramers, J.D., 1975. Approximation of terrestrial lead isotope evolution by a two-stage model. Earth Planet. Sci. Lett. 26, 207–221.

Storey, C.D., Jeffries, T.E., Smith, M., 2006. Common lead-corrected laser ablation ICPMS U-Pb systematics and geochronology of titanite. Chem. Geol. 227 (1–2), 37–52.

Thompson, K., Lawrence, D., Larson, D.J., Olson, J.D., Kelly, T.F., Gorman, B., 2007. In situ site-specific specimen preparation for atom probe tomography. Ultramicroscopy 107 (2–3), 131–139.

Thrane, K., Baker, J., Connelly, J., Nutman, A., 2005. Age, petrogenesis and metamorphism of the syn-collisional Prøven igneous complex, West Greenland. Contrib. Mineral. Petrol. 149, 541–555.

Tiepolo, M., Oberti, R., Vannucci, R., 2002. Trace-element incorporation in titanite: constraints from experimentally determined solid/liquid partition coefficients. Chem. Geol. 191 (1), 105–119.

Valley, J.W., Cavosie, A.J., Ushikubo, T., Reinhard, D.A., Lawrence, D.F., Larson, D.J., Clifton, P.H., Kelly, T.F., Wilde, S.A., Moser, D.E., 2014. Hadean age for a post-magma-ocean zircon confirmed by atom-probe tomography. Nat. Geosci. 7 (3), 219–223.

Valley, J.W., Reinhard, D.A., Cavosie, A.J., Ushikubo, T., Lawrence, D.F., Larson, D.J., Kelly, T.F., Snoeyenbos, D.R., Strickland, A., 2015. Presidential Address. Nano-and micro-geochronology in Hadean and Archean zircons by atom-probe tomography and SIMS: New tools for old minerals. Am. Mineral. 100 (7), 1355–1377.

White, L.F., Darling, J.R., Moser, D.E., Reinhard, D.A., Prosa, T.J., Bullen, D., Olson, D., Larson, D.J., Lawrence, D., Martin, I., 2017. Atomic-scale age resolution of planetary events. Nat. Commun. 8, 15597.

Wohlgemuth-Ueberwasser, C.C., Tegner, C., Pease, V., 2017. LA-Q-ICP-MS apatite U/Pb geochronology using common Pb in plagioclase: examples from layered mafic intrusions. Am. Mineral. 102, 571–579.